中国光学 (中英文) Chinese Optics 核心期刊

Refractive index sensor based on mode hybridized and multiple Fano resonances in a MIM waveguide coupled with dual D-shaped cavities

CHANG Xu-yan, QIU Yan-er, HAO Qi-ming, ZHANG Yan-jun, ZHAO Dong-qing, ZHANG Zhi-dong

Citation:
CHANG Xu-yan, QIU Yan-er, HAO Qi-ming, ZHANG Yan-jun, ZHAO Dong-qing, ZHANG Zhi-dong. Refractive index sensor based on mode hybridized and multiple Fano resonances in a MIM waveguide coupled with dual D-shaped cavities[J]. *Chinese Optics*, In press. doi: 10.3724/CO.EN-2026-0018
常旭艳, 邱炎儿, 郝启明, 张彦军, 赵冬青, 张志东. 基于MIM波导耦合双D型腔结构的模式杂化及多重Fano共振折射率传感器[J]. 中国光学, 优先发表. doi: 10.3724/CO.EN-2026-0018

View online: https://doi.org/10.3724/CO.EN-2026-0018

文章编号　2097-1842（xxxx）x-0001-12

Refractive index sensor based on mode hybridized and multiple Fano resonances in a MIM waveguide coupled with dual D-shaped cavities

CHANG Xu-yan[1], QIU Yan-er[2], HAO Qi-ming[1], ZHANG Yan-jun[1], ZHAO Dong-qing[1 *], ZHANG Zhi-dong[1]

（1. *Key Laboratory of Instrumentation Science & Dynamic Measurement of Ministry of Education*, *North University of China*, *Taiyuan* 030051, *P.R. China*;

2. *Department of Physics and Electronic Information Engineering*, *Lyuliang University*, *Lyuliang* 033001, *P.R. China*）

* *Corresponding author*, *E-mail*: *hunterdq@nuc.edu.cn*

Abstract: A multiple Fano resonance refractive index sensor based on metal-insulator-metal (MIM) waveguides coupled with dual D-shaped cavities is proposed. The transmission spectra and steady-state magnetic field distributions were simulated using the finite element method (FEM). The results show that the multiple distinct Fano resonances are observed, which are primarily attributed to mode hybridization between the vibration modes generated by the upper and lower D-shaped resonant cavities. Meanwhile, the influence of the geometric parameters of the D-shaped cavity on the Fano resonance was systematically investigated. Furthermore, the performance of the refractive index sensor based on multiple Fano resonances was evaluated. The results indicate that the sensor demonstrates excellent refractive index sensing performance, with a maximum sensitivity and a figure of merit reaching 1860 nm/RIU and 68.77 RIU^{-1}, respectively. This work provides a theoretical basis for the design of high-performance nanophotonic devices.

Key words: MIM waveguide; dual D-shaped cavities; fano resonance; mode hybridization; refractive index sensor

收稿日期:2020-01-03; **修订日期:**2020-01-05

基金项目:“三晋英才”计划科技创新青年拔尖人才项目 (No. 1012631) 资助

Supported by the Young Top-notch Talents in Science and Technology Innovation of the ‘San Jin Ying Cai’ Plan (Grant No. 1012631)

基于 MIM 波导耦合双 D 型腔结构的模式杂化及多重 Fano 共振折射率传感器

常旭艳[1], 邱炎儿[2], 郝启明[1], 张彦军[1], 赵冬青[1*], 张志东[1]
（1. 中北大学 仪器科学与动态测试教育部重点实验室, 山西 太原 030051；
2. 吕梁学院 物理与电子信息工程系, 山西 吕梁 033001）

摘要: 本文提出了一种基于金属-绝缘体-金属（MIM）波导耦合双 D 型谐振腔的多重 Fano 共振折射率传感器。采用有限元法（FEM）对其透射光谱和稳态磁场分布进行了仿真计算。结果表明，该结构中观测到了多重显著的 Fano 共振现象，这主要归因于上下 D 型谐振腔所产生的共振模式之间的模式杂化效应。同时，本文系统探究了 D 型谐振腔几何参数对 Fano 共振特性的影响。此外，对基于多重 Fano 共振的折射率传感器性能进行了评估。结果表明，该传感器展现出优异的折射率传感性能，其最大灵敏度（S）和品质因数（FOM）分别高达 1860 nm/RIU 和 68.77 RIU^{-1}。该研究工作为高性能纳米光子器件的设计提供了理论基础。

关　键　词: MIM 波导；双 D 形腔；法诺共振；模式杂化；折射率传感器
中图分类号: O482.31　　**文献标志码:** A　　**doi:** 10.3724/CO.EN-2026-0018　　**CSTR:** 32171.14.CO.EN-2026-0018

1 Introduction

Surface plasmon polaritons (SPPs) are hybrid electromagnetic modes confined at the metal-dielectric interface, formed by the coupling of electromagnetic fields with the collective oscillation of free electrons. They propagate along the interface and exhibit exponential decay in the perpendicular direction [1-3]. This unique property enables SPPs to confine electromagnetic energy to the deep-subwavelength scale, thereby overcoming the diffraction limit of conventional optics [4-5]. As a result, MIM waveguides, which serve as fundamental platforms for SPP propagation, have become essential components in high-density photonic integrated circuits. They provide the foundation for a variety of nanophotonic devices, including filters [6-8], beam splitters [9], and refractive index sensors [10-12].

In MIM waveguide-based sensing applications, the Fano resonance mechanism has garnered widespread attention due to its superior performance compared to conventional Lorentzian profiles. Physically, Fano resonance originates from the coherent interference between narrowband discrete states (typically supported by the resonator) and broadband continuous states (provided by the bus waveguide). This resonance mechanism exhibits high sensitivity to variations in both the structural parameters of the resonator and the surrounding dielectric environment [13-14]. In pursuit of enhanced sensing performance, researchers have not only proposed innovative single-cavity designs such as split-ring resonators [15-16] and semicircular cavities [17-18], but also developed composite resonance structures featuring stubs [19-21]. These designs substantially strengthen light-matter interactions, thereby positioning MIM waveguide-based sensors with exceptional potential for applications in biochemical detection, environmental monitoring, and temperature sensing [10,22-24]. However, these designs face notable challenges in practice. First, the quest for high sensitivity often employs complex nanopatterns, raising fabrication cost and difficulty while reducing reproducibility. Second, ohmic losses in metals limit the FOM. Thus, achieving a compact, easily fabricated plasmonic sensor with both ultrahigh sensitivity and high FOM remains a critical pursuit in nanophotonics.

In this paper, we propose a plasmonic sensing structure based on a MIM waveguide coupled to dual D-shaped cavities. Utilizing the finite element method, we demonstrate that this compact structure can generate multiple Fano resonances across the visible to near-infrared wavelength range. By analyzing the steady-state magnetic field distribution, we elucidate the physical formation mechanism of these resonances, revealing that the multiple Fano resonances arise from the coupling between the waveguide and the cavities as well as the coupling between the two D-shaped cavities. In addition, we discuss the influence of geometric parameter variations on the Fano resonances and comprehensively evaluate the sensing performance of the device by changing the refractive index of the filling medium. Most importantly, the proposed sensor exhibits excellent sensing capabilities, making it highly suitable for high-performance refractive index sensing applications.

2 Structural Model and Analysis Method

Figure 1 shows the two-dimensional schematic of the proposed MIM waveguide-based refractive index sensor, consisting of a MIM waveguide and two symmetrically placed D-shaped resonant cavities. The green and white regions represent silver (Ag) and air, respectively. Silver is selected for its excellent optical properties in the visible to near-infrared range, including strong electric field enhancement and low ohmic losses. In addition, the D-shaped resonators feature a simple geometry that facilitates fabrication. To ensure that only the fundamental transverse magnetic mode (TM_0) is supported, both the waveguide and resonator widths are fixed at w = 50 nm. The default geometric parameters are as follows: $r_1 = (R_1 + R_2)/2$ = 155 nm, $r_2 = (R_3 + R_4)/2$ = 155 nm, $l_1 = l_2$ = 160 nm, g = 10 nm, d = 10 nm.

Silver is selected as the metallic material for this structure, and a modified Debye model [25-26] is employed to accurately characterize its optical properties in the near-infrared region. The frequency-dependent relative permittivity of silver, denoted as $\varepsilon(\omega)$, is expressed as follows:

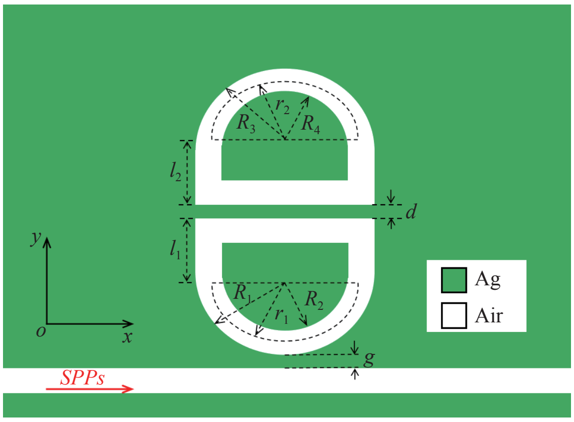

Fig. 1 Schematic diagram of the MIM waveguide coupled with dual D-shaped cavities.

$$\varepsilon(\omega) = \varepsilon_\infty + \frac{(\varepsilon_s - \varepsilon_\infty)}{1 + i\omega\tau} + \frac{\sigma}{i\omega\varepsilon_0} \quad . \qquad (1)$$

In this equation, the infinite-frequency permittivity $\varepsilon_\infty = 3.8344$, the static permittivity $\varepsilon_s = -9530.5$, the relaxation time $\tau = 7.35 \times 10^{-15}$ s, and the electrical conductivity of silver $\sigma = 1.1486 \times 10^7$ S/m.

The optical properties of the MIM waveguide coupled cavity were numerically analyzed using the finite element method (FEM), and the perfectly matched layers (PMLs) were applied. The transmittance of the system was calculated using the expression T = $|S_{21}|^2$, where S_{21} denotes the transmission coefficient from the input port to the output port [27].

The dispersion relation of the MIM waveguide can be expressed as [28]:

$$\tanh(\kappa w) = 2\kappa p\alpha / (\kappa^2 + p^2\alpha^2) \quad , \qquad (2)$$

Here, κ denotes the transverse wave vector in the MIM waveguide. The parameters are defined as $p = \varepsilon_{in}/\varepsilon_m$ and $\alpha = [k_0^2(\varepsilon_{in} - \varepsilon_m) + \kappa^2]^{1/2}$, where ε_{in} and ε_m represent the relative permittivities of the insulator and metal, respectively, and $k_0 = 2\pi/\lambda_0$ is the free-space wave vector. The value of κ can be determined by solving this equation using an iterative method. Subsequently, the effective refractive index (n_{eff}) of the MIM waveguide is calculated as

$n_{eff} = [\varepsilon_m + (\kappa/k_0)^2]^{1/2}$, and the SPP wavelength is expressed as $\lambda_{spp} = \lambda_0/Re(n_{eff})$. So the resonant mode number m supported within the cavity can be defined as:

$$m = \frac{L_{eff}}{\lambda_{\text{spp}}} \quad . \tag{3}$$

Inaddition, the sensitivity (S) [29] and figure of merit (FOM) [30], are adopted to evaluate the sensing performance. They are expressed as follows:

$$S = \frac{\Delta\lambda}{\Delta n} \quad , \tag{4}$$

$$FOM = \frac{S}{FWHM} \quad , \tag{5}$$

Here, $\Delta\lambda$ represents the resonance wavelength shift, and Δn denotes the change in the refractive index of the sensing medium [31]. $FWHM$ is the full width at half maximum of the resonance dip, given by $FWHM = \lambda_b - \lambda_a$, where λ_a and λ_b are the wavelengths at which transmissivity equals (T_{max} + T_{min})/2. T_{max} and T_{min} are the peak and dip transmissivity, respectively[32].

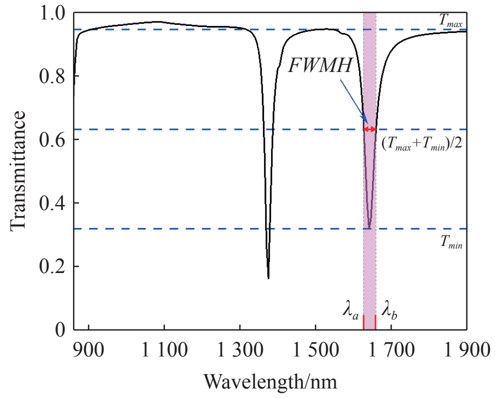

Fig. 2 The diagram of $FWHM$.

3 Results and Discussion

To investigate the formation mechanism of the Fano resonance and the advantages of the proposed structure, this study examines a single bus waveguide, followed by its coupled configurations with a single D-shaped cavity (including two coupling modes: the curved edge of the cavity adjacent to the waveguide (CEC) and the straight edge adjacent to the waveguide (SEC)) and dual D-shaped cavities. Their transmission spectra are presented in Figure 3. For the bus waveguide (blue solid line), the transmittance remains high (approximately 0.9-0.95) across the entire simulated wavelength range, exhibiting a flat and broadband spectral response that corresponds to the continuous waveguide mode of the system. In contrast, the CEC structure (red solid line) exhibits two sharp transmission dips at λ_1 = 1 455 nm and λ_2 = 735 nm, while the SEC structure (purple solid line) shows two transmission dips at λ_3 = 1 485 nm and λ_4 = 790 nm. The formation of these Fano resonance dips is the result of interference between the broadband continuous mode provided by the bus waveguide and the narrowband discrete resonant modes excited by the D-shaped cavity.

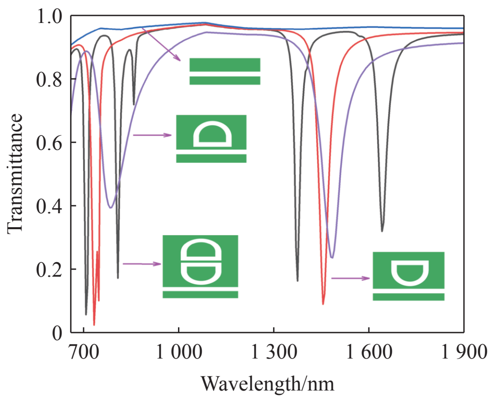

Fig. 3 Transmission spectra for four distinct configurations.

To further enhance the sensing performance, a second D-shaped cavity was introduced to construct a dual-cavity coupled system, with its transmission spectrum depicted by the black solid line in Figure 3. Compared with the single-cavity configuration, the dual-cavity structure produces more transmission dips. These dips also exhibit a narrower $FWHM$, which improves the FOM. Furthermore, the dips shift toward longer wavelengths. A longer resonance wavelength corresponds to a larger penetration depth and interaction volume, thus yielding higher refractive index sensitivity.

To elucidate the physical mechanism underlying the Fano resonance in this structure, the normalized magnetic field distributions at four Fano resonance dips (λ = 1 640 nm (FR1), λ = 1 375 nm (FR2), λ = 810 nm (FR3) and λ = 710 nm (FR4)) were calculated, as shown in Figures 4(a)-(d). The length of the coupled cavity is $L_{eff}=\pi r_1+2(l_1-w/2)+2r_1=1\,066.7$ nm. At λ = 1 640 nm and λ = 1 375 nm, Re(n_{eff}) is 1.388 and 1.392, corresponding to λ_{spp} of 1 181 nm and 988 nm, respectively. Calculations using Equation (3) yield resonance mode numbers of approximately 0.90 and 1.08 for the D-shaped resonator, respectively. Both values are close to the integer 1, indicating that these two resonance dips correspond to first-order modes. This theoretical result is consistent with the magnetic field mode distributions, as shown in Figures 4(a) and 4(b). At λ = 1 640 nm, the magnetic field polarities in the upper and lower D-shaped cavities exhibit an anti-symmetric distribution. The anti-phase magnetic field distribution corresponds to co-aligned electric dipole moments, causing opposite charges to accumulate on either side of the gap. The mutual attraction between opposite charges forms a strong coupling region, which increases the electron oscillation distance within the resonator. This causes the resonance wavelength of the coupled structure to redshift relative to the single-cavity mode, resulting in a first-order anti-symmetric mode. In contrast, at λ = 1 375 nm, the magnetic field polarities in the upper and lower D-shaped cavities exhibit a symmetric distribution. The in-phase magnetic field distribution corresponds to anti-aligned electric dipole moments, causing like charges to accumulate on either side of the gap. The repulsion between like charges shortens the electron oscillation path, causing the resonance wavelength to blueshift relative to the single-cavity mode, thereby forming the first-order symmetric mode.

At λ = 810 nm and λ = 710 nm, Re(n_{eff}) is 1.417 and 1.430, with λ_{spp} of 572 nm and 496 nm, respectively. Using Equation (3), the resonance mode numbers are calculated to be approximately 1.86 and 2.14, respectively, which are close to the integer 2. This theoretical result agrees with the field distributions shown in Figures 4(c)–(d), where the dips correspond to the second-order antisymmetric and symmetric modes, respectively, through the same mechanisms as the first-order modes.

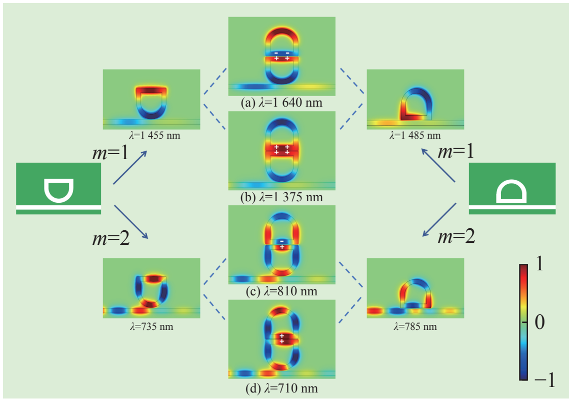

Fig. 4　Mode Hybridization in a Double-D-Shaped Cavity Waveguide Coupling System, (a) λ = 1 640 nm, (b) λ = 1 375 nm, (c) λ = 810 nm, (d) λ = 710 nm.

To investigate the influence of geometric dimensions of the D-shaped resonator on the Fano resonance characteristics, the transmission spectra of the proposed structure were systematically calculated and analyzed under various parameter configurations. Initially, the radii r_1 and r_2 of the two D-shaped cavities were individually varied from 135 nm to 175 nm in steps of 10 nm, tuning only one parameter at a time while keeping all other geometric dimensions constant. As shown in Figures 5(a) and 6(a), regardless of whether the radius r_1 and r_2 are increased, all resonance wavelengths exhibit a significant redshift. This phenomenon can be attributed to the increased effective optical path length with larger cavity circumference. However, the resonance dips display markedly different sensitivities to geometric variations. As illustrated in Figures 5(b) and 6(b), with increasing r_1 and r_2, the redshift rates of FR1 and FR2 are substantially higher than those of the other two resonance dips. This behavior is closely related to the resonance mode order. According to plasmon resonance theory, the resonance wavelength of the resonator is inversely proportional to the mode order. Consequently, lower-order modes—particularly the first-order mode—exhibit greater sensitivity to changes in geometric parameters compared to higher-order modes.

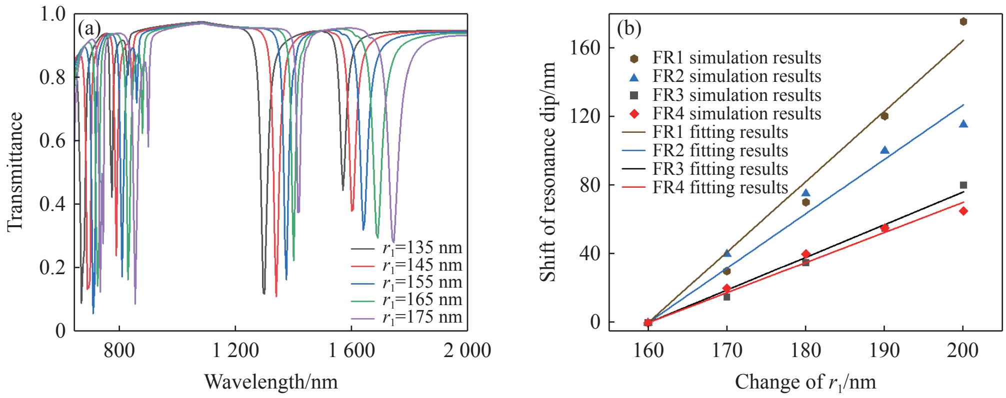

Fig. 5 (a) Transmission spectra of the MIM waveguide coupled with dual D-shaped cavities for different r_1; (b) Shift of the resonance dip as a function of r_1.

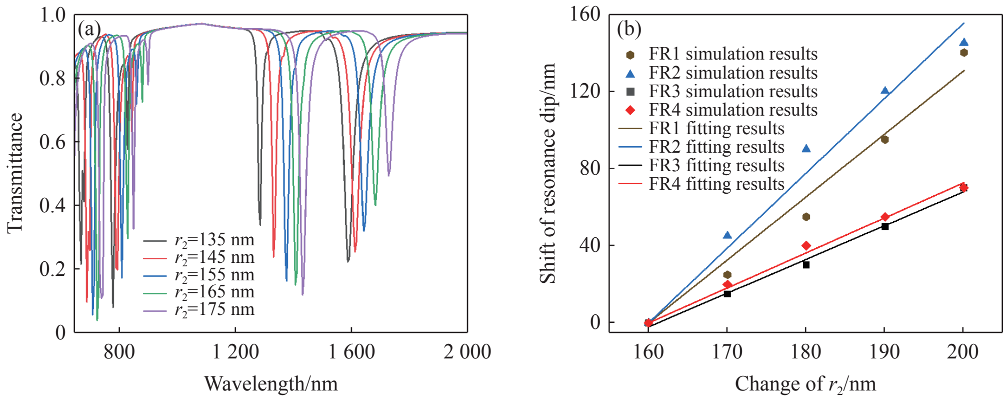

Fig. 6 (a) Transmission spectra of the MIM waveguide coupled with dual D-shaped cavities for different r_2; (b) Shift of the resonance dip as a function of r_2.

Furthermore, as r_1 increases, the first-order anti-symmetric mode (FR1) experiences a faster redshift than the symmetric mode (FR2). During this process, the transmittance of FR1 gradually decreases, whereas that of FR2 gradually increases. A similar trend is observed for the higher-order modes, where the redshift rate of the second-order anti-symmetric mode (FR3) exceeds that of the symmetric mode (FR4). Conversely, as r_2 increases, the redshift of the first-order symmetric mode (FR2) outpaces that of the anti-symmetric mode (FR1). Consequently, the transmittance of FR2 gradually decreases, while that of FR1 gradually increases. Correspondingly, the redshift rate of the second-order symmetric mode (FR4) is faster than that of the anti-symmetric mode (FR3). This is because the first-order FR1 and second-order FR3 resonance modes depend primarily on the structural parameters of the lower D-shaped cavity, whereas the first-order FR2 and second-order FR4 are mainly determined by the resonance of the surface plasmon polaritons (SPPs) coupled from the lower D-shaped cavity to the upper D-shaped cavity. Therefore, as r1 increases, the redshift rates are: FR1 > FR2, FR3 > FR4. As r_2 increases, the redshift rates are: FR2 > FR1, FR4 > FR3. Regarding changes in transmittance, as the radius r_1 of the lower cavity increases, the structural symmetry between the upper and lower D-shaped cavities is broken. This symmetry breaking leads to changes in the energy distribution within the system and in the phase interference conditions. As r_1 increases, the length of the lower D-shaped cavity increases, strengthening the coupling between the main waveguide and the lower cavity. Consequently, more energy is coupled and localized within the lower cavity, causing the transmittance of FR1 to decrease. At the same time, because the lower cavity increases in size while the upper cavity remains unchanged, the asymmetric structure induces a resonance wavelength mismatch between the upper and lower cavities. Consequently, the amount of energy that can be coupled into the upper cavity decreases, leading to an increase in the transmittance of FR2. Conversely, when the dimensions of the lower D-shaped cavity remain constant, the effective optical path length of the upper cavity increases with parameter r_2. More energy is coupled through the lower cavity and localized in the upper cavity, causing the corresponding transmittance of FR2 to decrease. Concurrently, since a large amount of energy is coupled into the upper cavity, the energy in the lower cavity decreases, leading to an increase in the transmittance of FR1.

Subsequently, the effects of the geometric parameters l_1 and l_2 on the transmission spectra were investigated by varying both values from 140 nm to 180 nm in steps of 10 nm, tuning only one parameter at a time. The transmission spectra are shown in Figure 7 and Figure 8. Regardless of whether l_1 or l_2 is increased, all resonance dips exhibit a significant redshift. However, the overall redshift rates induced by increasing l_1 or l_2 are considerably lower than those caused by increasing r_1 or r_2. This is because, for the same parameter increment, the increase in the cavity's perimeter driven by linear parameters l_1 or l_2 is smaller than that driven by radial parameters, resulting in a more modest wavelength redshift.

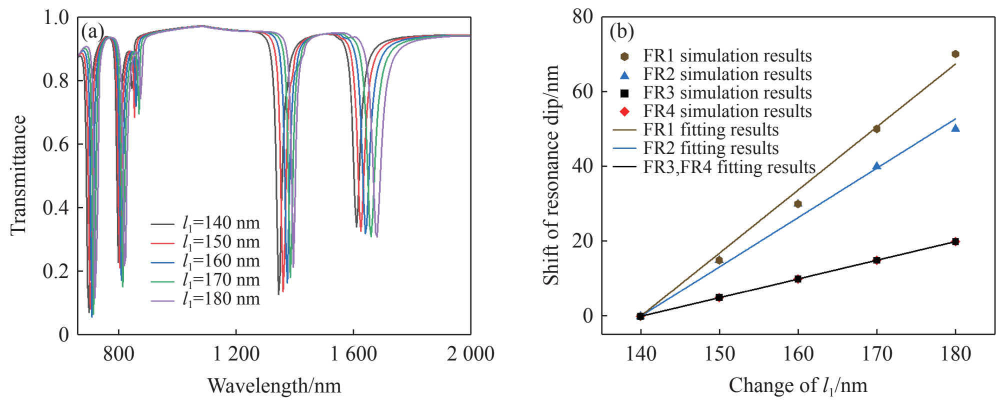

Fig. 7 (a) Transmission spectra of the MIM waveguide coupled with dual D-shaped cavities for different l_1; (b) Shift of the resonance dip as a function of l_1.

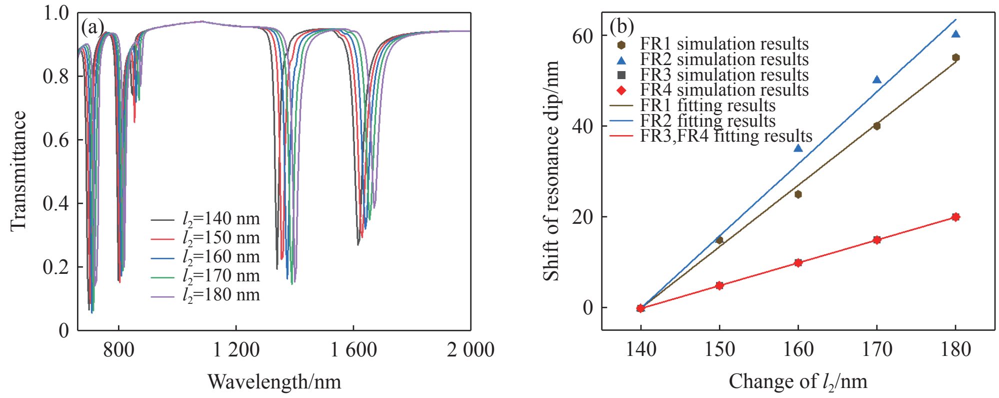

Fig. 8 (a) Transmission spectra of the MIM waveguide coupled with dual D-shaped cavities for different l_2; (b) Shift of the resonance dip as a function of l_2.

We further investigate the effect of the gap g between the MIM waveguide and the D-shaped resonator on the system's transmission characteristics. Figure 9(a) presents the transmission spectra obtained by varying g from 10 nm to 30 nm in 5-nm increments. The results show that all resonance dips blueshift to varying degrees, and the blueshift gradually saturates as g increases, as shown in Figure 9(b).

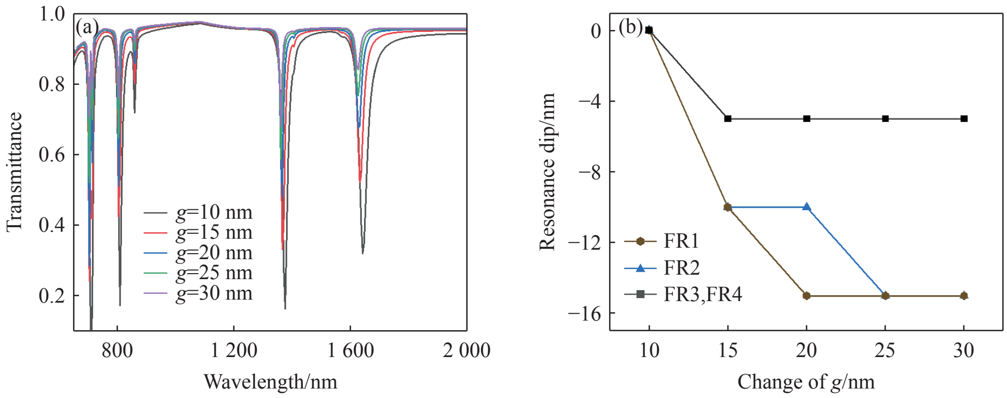

Fig. 9 (a) Transmission spectra of the MIM waveguide coupled with dual D-shaped cavities for different g; (b) Shift of the resonance dip as a function of g.

The physical origin of this blueshift phenomenon lies in the change in the coupling phase between the waveguide and the cavity. In plasmonic coupling systems, the generation of resonance requires the following phase-matching conditions to be satisfied:

$$\frac{4\pi n_{eff} L_{eff}}{\lambda} + \phi_r + \phi_c = 2m\pi \quad , \qquad (6)$$

In this equation, n_{eff} represents the effective refractive index within the cavity, L_{eff} is the characteristic length of the resonator, λ is the resonant wavelength, ϕ_r and ϕ_c denote the interface reflection phase and the additional phase delay introduced by coupling, respectively, and m is the resonant mode number. As g increases, the near-field interaction between the waveguide and the resonator weakens, leading to a corresponding decrease in the coupling phase ϕ_c. According to the equation, the resonance wavelength λ decreases, which manifests as a blueshift in the transmission spectrum. When g exceeds the decay length of the surface plasmon evanescent field, the near-field perturbation of the bus waveguide on the resonator system significantly weakens, and the resonance wavelength is no longer affected by the position of the external waveguide, leading to saturation of the shift. Furthermore, as g increases, the transmittance at the four Fano resonance dips gradually increases. This occurs because the coupling efficiency decreases exponentially with increasing separation, causing more photons to transmit directly through the bus waveguide and thereby diminishing the Fano resonance intensity.

The transmission spectra were calculated by varying the parameter d from 10 nm to 30 nm in steps of 5 nm, as shown in Figure 10(a). With increasing d, FR2 and FR4 exhibit a redshift, whereas FR1 and FR3 display a significant blueshift. As illustrated in Figure 10(b), the blueshift fitting curves for FR1 and FR3 present a nonlinear deceleration trend, indicating that the blueshift rates of these two resonance dips gradually diminish. For the antisymmetric modes FR1 and FR3, an increase in d mitigates the attractive force between opposite charges. This shortens the effective electron oscillation path within the cavity, thereby inducing a blueshift. Conversely, for the symmetric modes FR2 and FR4, an increase in d weakens the repulsion between like charges. This extends the effective electron oscillation path within the cavity, ultimately causing a redshift.

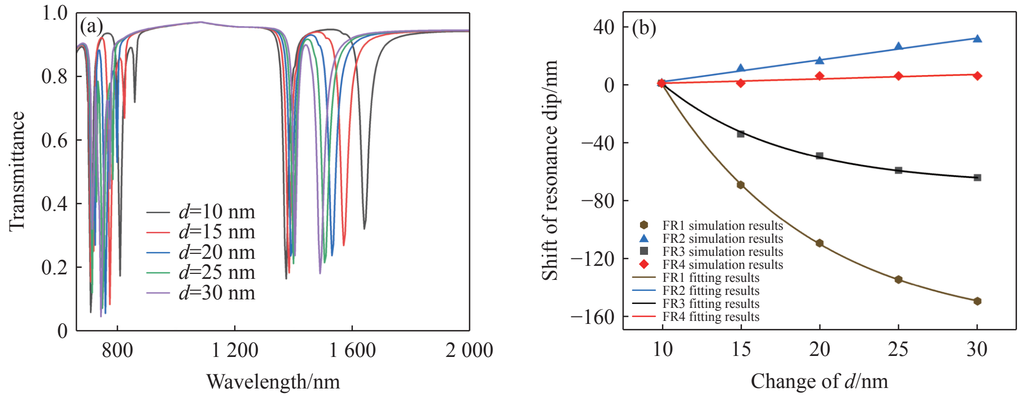

Fig. 10　(a) Transmission spectra of the MIM waveguide coupled with dual D-shaped cavities for different *d*; (b) Shift of the resonance dip as a function of *d*.

To further investigate the influence of the medium's refractive index n on the transmission characteristics of the waveguide, the transmission spectra were calculated for various refractive index values. While keeping all other geometric parameters constant, the refractive index n was gradually increased from 1.00 to 1.20 in steps of 0.05. As shown in Figure 11(a), all Fano resonance wavelengths redshift significantly with increasing refractive index, indicating that the resonance wavelengths are highly sensitive to changes in the surrounding medium. The relationship between the central wavelength of each resonance dip and the refractive index was extracted and fitted linearly, as presented in Figure 11(b). The results demonstrate that all resonance wavelengths possess an excellent linear correlation with the refractive index: R^2_{FR1} = 0.992 65, R^2_{FR2} = 0.999 62, R^2_{FR3} = 0.999 31, R^2_{FR4} = 0.99914. The performance of surface plasmon sensors is primarily evaluated using two key metrics: sensitivity (*S*) and figure of merit (*FOM*). Based on Equation (4), the sensitivities of FR1, FR2, FR3 and FR4 are calculated to be 1860, 1 350, 760 and 680 nm/RIU, respectively. Similarly, using Equation (5), their corresponding *FOM* values are determined as 57.25, 68.77, 56.69, and 48.97 RIU^{-1}, respectively.

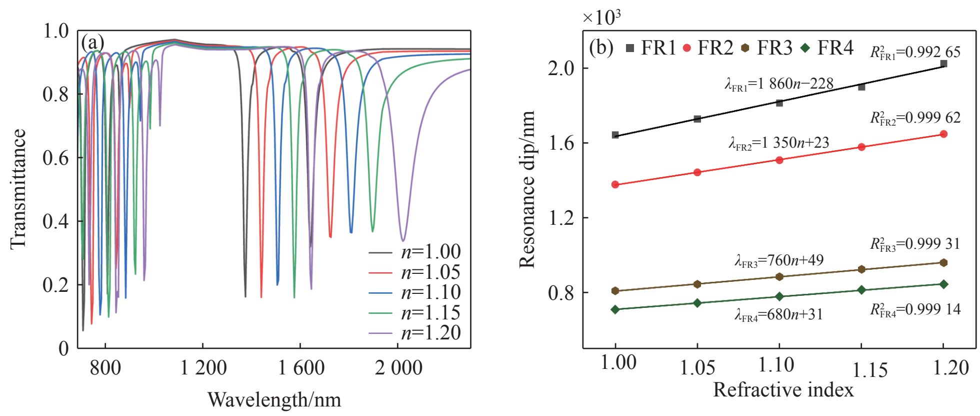

Fig. 11　(a) Transmission spectra as a function of refractive index; (b) linear fit of the resonance dip wavelength versus refractive index.

Finally, the performance of the proposed sensor is compared with that of previously reported structures, as summarized in Table 1. The results demonstrate that the proposed design significantly outperforms many existing sensors of the same type in terms of overall sensing performance.

Tab. 1 Comparison of the proposed sensor with other reported plasmonic sensors.

Reference	Resonator structure	S (nm/RIU)	FOM (RIU^{-1})
[16]	circular split ring	1250	54
[17]	semicircular cavity	941.33	-
[31]	a nanoring	567.2	3.72
[33]	square shaped cavity	1210.12	20
[34]	dual-ring resonator	324.76	10.187
[35]	arc-shaped resonator	867.20	57.80
[36]	L-shaped resonator	1638	21.84
[37]	semi-elliptical ring resonator	1783	27
This work	dual D-shaped cavities	1860,1350,760,680	57.25,68.77, 56.69,48.97

4 Conclusion

This paper proposes and systematically investigates a surface plasmon refractive index sensor based on the coupling between a MIM waveguide and dual D-shaped resonators. Numerical simulations using the finite element method confirm that the proposed structure excites multiple distinct Fano resonances in the near-infrared region. By analyzing the transmission spectra of different structures and the magnetic field distributions at the wavelengths corresponding to different Fano resonance dips, the generation mechanism of the Fano resonances in the proposed structure is elucidated. The coupling between the upper and lower D-shaped cavities induces mode hybridization. Furthermore, the effects of varying structural parameters on different Fano resonance dips are investigated. In terms of refractive index sensing performance, the proposed structure exhibits an excellent linear response to variations in the surrounding medium. The sensor achieves a maximum sensitivity (*S*) of 1860 nm/RIU (from FR1) and a *FOM* of 68.77 RIU^{-1} (from FR2), demonstrating overall sensing performance that significantly surpasses that of many existing structures of the same type. In terms of fabrication, high-quality silver films can be deposited on smooth substrates using magnetron sputtering technology, followed by precise patterning employing mature processing techniques such as electron beam lithography (EBL) or focused ion beam (FIB) etching. This study provides a solid theoretical foundation and design strategy for the development of on-chip high-sensitivity biochemical sensors and micro-nano photonic devices.

References:

[1] HU F F, YI H X, ZHOU ZH P. Band-pass plasmonic slot filter with band selection and spectrally splitting capabilities[J]. *Optics Express*, 2011, 19(6): 4848-4855.

[2] BARNES W L, DEREUX A, EBBESEN T W. Surface plasmon subwavelength optics[J]. *Nature*, 2003, 424(6950): 824-830.

[3] HADDOUCHE L, CHERBI L. Comparison of finite element and transfer matrix methods for numerical investigation of surface plasmon waveguides[J]. *Optics Communications*, 2017, 382: 132-137.

[4] HAN ZH H, BOZHEVOLNYI S I. Radiation guiding with surface plasmon polaritons[J]. *Reports on Progress in Physics*, 2013, 76(1): 016402.

[5] REN X B, REN K, CAI Y X. Tunable compact nanosensor based on Fano resonance in a plasmonic waveguide system[J]. *Applied Optics*, 2017, 56(31): H1-H9.

[6] TUHIN S S, ROUF H K. High-performance MIM plasmonic notch filters based on ring resonators using phase-change-materials[J]. *Plasmonics*, 2025, 20(7): 4821-4833.

[7] SONG J Q, TIAN H, HAO Y, *et al.*. A tunable low-pass filter based on MIM structure with kerr effect[J]. *Plasmonics*, 2025, 20(5): 2625-2633.

[8] KORKMAZ S. Multiple ultra-narrow band-stop filters based on MIM plasmonic waveguide with nanoring cavities[J]. *Physica Scripta*, 2024, 99(3): 035503.

[9] NANDA R, RATH R, SWARNAKAR S, *et al.*. Design of all-optical directional coupler using plasmonic MIM waveguide for switching applications[J]. *Plasmonics*, 2022, 17(5): 2153-2159.

[10] YADAV G K, SARKAR D, METYA S K. High FOM plasmonic nanosensor for blood biomolecule detection[J]. *Plasmonics*, 2025, 20(5): 2655-2663.

[11] LIU W X, YAN SH B, XU ZH Y, *et al*.. Plasmonic sensor based on an MIM waveguide coupled with a ring–bridge–rounded square resonator[J]. *Photonics*, 2025, 13(1): 34.

[12] YAN ZH K, YAN SH B, XU Z H, *et al*.. Multi-structure-based refractive index sensor and its application in temperature sensing[J]. *Sensors*, 2025, 25(2): 412.

[13] XU D J, YAN SH B, YANG X Y, *et al*.. A nanoscale structure based on a ring with matchstick-shape cavity for glucose concentration and temperature detection[J]. *IEEE Sensors Journal*, 2021, 21(4): 4442-4450.

[14] 张志东, 张慧男, 梁洁, 等. 基于 Au 纳米平行双棒超表面阵列的双 Fano 共振和折射率传感器特性研究[J]. 中国光学 (中英文), 2023, 16(4): 961-971.

ZHANG ZH D, ZHANG H N, LIANG J, *et al*.. Double Fano resonance and refractive index sensors based on parallel-arranged Au nanorod dimer metasurface arrays[J]. *Chinese Optics*, 2023, 16(4): 961-971. (in Chinese).

[15] CHEN J F, LIAN X Y, ZHAO M, *et al*.. Multimode Fano resonances sensing based on a non-through MIM waveguide with a square split-ring resonance cavity[J]. *Biosensors*, 2022, 12(5): 306.

[16] ZHU J, XU Q N, JIAN ZH H. Novel high performance Fano resonance sensor with circular split ring resonance[J]. *Physica B: Condensed Matter*, 2024, 689: 416205.

[17] BUTT M A, KAZANSKIY N L, KHONINA S N. Metal-insulator-metal waveguide plasmonic sensor system for refractive index sensing applications[J]. *Advanced Photonics Research*, 2023, 4(7): 2300079.

[18] CHEN J H, WANG L, FENG Y T, *et al*.. A nano-refractive index sensor based on a MIM waveguide with a semicircular ring rectangular resonator[J]. *Micro and Nanostructures*, 2024, 186: 207730.

[19] MOEINIMALEKI B, KAATUZIAN H, MALLAH LIVANI A, *et al*.. Plasmonic refractive index nano sensor based on triplet coupled stub resonators based Fano resonances[J]. *IET Optoelectronics*, 2023, 17(6): 257-272.

[20] YAN SH B, SHI H R, YANG X Y, *et al*.. Study on the nanosensor based on a MIM waveguide with a stub coupled with a horizontal b-type cavity[J]. *Photonics*, 2021, 8(4): 125.

[21] CAO Y H, YAN SH B, LIU F, *et al*.. Nanoscale refractive index sensor based on an MIM waveguide coupled to U-shaped ring resonator with three stubs for alcohol solution concentration detection[J]. *Plasmonics*, 2024, 19(5): 2421-2432.

[22] BUTT M A. Numerical assessment of a metal-insulator-metal waveguide-based plasmonic sensor system for the recognition of tuberculosis in blood plasma[J]. *Micromachines*, 2023, 14(4): 729.

[23] BUTT M A. Plasmonic sensor system embedded with orthogonal mode couplers for simultaneous monitoring of temperature and refractive index[J]. *Plasmonics*, 2025, 20(1): 459-469.

[24] GHANAVATI M, KARAMI M A. Ellipsoid defect in trapezoidal-shaped cavities coupled to multi-resonance plasmonic metal–insulator-metal waveguide toward ultrasensitive temperature sensor[J]. *Plasmonics*, 2023, 18(3): 1047-1057.

[25] ZAYATS A V, SMOLYANINOV I I, MARADUDIN A A. Nano-optics of surface plasmon polaritons[J]. *Physics Reports*, 2005, 408(3-4): 131-314.

[26] GAI H F, WANG J, TIAN Q. Modified Debye model parameters of metals applicable for broadband calculations[J]. *Applied Optics*, 2007, 46(12): 2229-2233.

[27] ZHANG ZH D, LUO L, XUE CH Y, *et al*.. Fano resonance based on metal-insulator-metal waveguide-coupled double rectangular cavities for plasmonic nanosensors[J]. *Sensors*, 2016, 16(5): 642.

[28] ZHANG ZH Y, WANG J D, ZHAO Y N, *et al*. . Numerical investigation of a branch-shaped filter based on metal-insulator-metal waveguide[J]. *Plasmonics*, 2011, 6(4): 773-778. **(查阅网上资料, 未能确认标黄作者信息, 请确认)**.

[29] LIU X, LI J N, CHEN J F, *et al*. . Independently tunable triple Fano resonances based on MIM waveguide structure with a semi-ring cavity and its sensing characteristics[J]. *Optics Express*, 2021, 29(13): 20829-20838. **(查阅网上资料, 未能确认标黄作者信息, 请确认)**.

[30] BUTT M A, KAZANSKIY N L, KHONINA S N. Highly sensitive refractive index sensor based on plasmonic bow tie configuration[J]. *Photonic Sensors*, 2020, 10(3): 223-232.

[31] SHOKORLOU Y M, HEIDARZADEH H, BAHADOR H. Simulation and analysis of ring shape metal–insulator-metal plasmonic biosensors for the detection of prostate-specific antigen (PSA)[J]. *Plasmonics*, 2022, 17(5): 2197-2204.

[32] SRIVASTAVA A, VERMA A, PRAJAPATI Y K. Theoretical study of hazardous carbon-di-oxide gas sensing using

MIM structure-based SPR sensing scheme[J]. *IET Optoelectronics*, 2021, 15(4): 167-177.

[33] GHANAVATI M, KARAMI M A. Plasmonic CH_4 sensor based on MIM waveguide coupled to circular nanorod in a square-shaped cavity[J]. *IET Optoelectronics*, 2025, 19(1): e70002.

[34] KHODAIE A, RAFIGHIRANI Y, HEIDARZADEH H, *et al*.. Design of a plasmonic optical biosensor based on a metal-insulator-metal ring resonator for the detection of various bacterial pathogens[J]. *Scientific Reports*, 2025, 15(1): 20699.

[35] TANG X Y, LI Y CH, CHEN F, *et al*.. Gas concentration and refractive index sensor based on plasmonic induced absorption in metal-insulator-metal waveguide coupled with arc resonators structure[J]. *Physica Scripta*, 2024, 99(6): 065561.

[36] RAHAD R, HOSSAIN N, HOSSAIN A. Enhanced alcohol detection using surface plasmon polariton dependent MIM plasmonic sensor[J]. *Plasmonics*, 2025, 20(3): 1331-1340.

[37] FIGUIGUE M, MAHBOUB O, EL HAFFAR R. Optical properties of multiple Fano resonance in MIM waveguide system coupled with a semi-elliptical ring resonator[J]. *Plasmonics*, 2024, 19(2): 721-732.

Author Biographies:

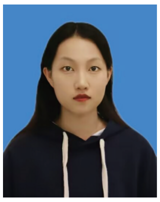

CHANG Xuyan (2000—), female, born in Xinzhou, Shanxi Province, is currently a master's student in Instrumentation Engineering at North University of China, having received her bachelor's degree from Shanxi University in 2023. E-mail: 1927744674@qq.com

ZHAO Dongqing (1975—), male, born in Jinzhong, Shanxi Province, received his Ph.D. degree from North University of China. He is currently an Associate Professor and Master Supervisor with the School of Instrument and Electronics, North University of China. His research interests include digital signal acquisition and data processing. E-mail: hunterdq@nuc.edu.cn